Article:
Spirito, D, von den Driesch, N, Manganelli, CL et al. (2021) Thermoelectric Efficiency of Epitaxial GeSn Alloys for Integrated Si-Based Applications: Assessing the Lattice Thermal Conductivity by Raman Thermometry. ACS Applied Energy Materials. ISSN: 2574-0962

https://doi.org/10.1021/acsaem.1c01576

Thermoelectric Efficiency of Epitaxial GeSn Alloys for Integrated Si-based Applications - Assessing the Lattice Thermal Conductivity by Raman Thermometry

Davide Spirito[1], Nils von den Driesch[2], Costanza Lucia Manganelli[1], Marvin Hartwig Zoellner[1], Agnieszka Anna Corley-Wiciak[1], Zoran Ikonic[3], Toma Stoica[4], Detlev Grützmacher[2], Dan Buca[2*] and Giovanni Capellini[1,5]*

[1]IHP – Leibniz-Institut für innovative Mikroelektronik, Im Technologiepark 25, 15236 Frankfurt (Oder), Germany

[2] Peter Grünberg Institute 9 (PGI-9) and JARA-Fundamentals of Future Information Technologies (JARA-FIT), Forschungszentrum Jülich, 52425 Jülich, Germany

[3]Pollard Institute, School of Electronic and Electrical Engineering, University of Leeds, Leeds LS2 9JT, UK

[4] National Institute of Materials Physics, 405A Atomistilor St., 077125 Magurele, Romania.

[5] Dipartimento di Scienze, Università Roma Tre, V.le G. Marconi 446, 00146 Roma, Italy.

KEYWORDS GeSn, Raman thermometry, Thermoelectric, Heat conduction, Thermal conductivity, Energy harvesting.

ABSTRACT. Energy harvesting for Internet of Things applications, comprising sensing, life sciences, wearables or communications, requires efficient thermoelectric (TE) materials, ideally semiconductors compatible with the Si technology. In this work, we investigate the potential of GeSn/Ge layers, a group IV material system, as TE material for low-grade heat conversion. We extract the lattice thermal conductivity, by developing an analytical model based on Raman thermometry and heat transport model, and use it to predict thermoelectric performances. The lattice thermal conductivity decreases from 56 W/m·K for Ge to 4 W/m·K by increasing Sn atomic composition to 14at.%. The bulk cubic Ge0.86Sn0.14 alloy features a TE figure of merit of ZT~0.4 at 300K and an impressive 1.04 at 600K. These values are extremely promising in view of the use of GeSn/Ge layers operating in the typical on-chip temperature range.

INTRODUCTION

Low-grade heat, in the temperature range of 300K to 600K, is one of the most abundant and wasted energy resources[1], being produced by e.g. electronic devices (smartphones, computers, etc.), in automotive systems, or by the human body[2]. In addition, thermoelectrics (TE) are becoming highly relevant for the implementation of Artificial Intelligence of Things (AIoT) vision, which requires self-powered devices for environmental and medical sensing, wearables, or communication applications.[3,4] Energy harvesting materials and technologies that can efficiently convert this energy into electricity are experiencing ever-growing interest. TE materials are evaluated by their figure of merit $ZT = \sigma S^2 T/\kappa$, where σ, S, T, and κ are electrical conductivity,

Seebeck coefficient, temperature, and thermal conductivity (the sum of the lattice and electronic components $\kappa = \kappa_{latt} + \kappa_e$), respectively. Traditional thermoelectric IV-VI chalcogenides sharing similar chemical and physical properties, such as GeTe, GeSe[5,6], SnTe[7], SnSe[8] - based materials, feature ZT >1 above 600K (peaking at 900K)[9,10] and, consequently, they are not suitable for low-grade waste heat recovery. Moreover, the practical use of IV-VI materials is limited due to difficult integration with the "standard" silicon (Si) complementary metal oxide semiconductors (CMOS) microelectronic technology.

A breakthrough in TE will be to synthesise a crystalline material fully compatible with CMOS, enabling the monolithic co-integration of electronics, photonics, and thermoelectrics on the same chip. Group IV elements, Si and Ge, are unbeatable in their abundance, biocompatibility and manufacturability, and feature excellent electrical properties. However, they show a large thermal conductivity resulting in small ZT<0.15 at T=300-400K, the typical operating temperature range of Si devices[11]. Typically the thermal conductivity can be reduced by using alloys, thus a solution for an efficient and Si-integrable TE material could leverage on the alloying of another group IV semiconductor, α-tin (Sn) with Ge or SiGe. Recently, epitaxial GeSn alloys have led to major advances in photonics, e.g. GeSn laser [12–14], and in nanoelectronics, e.g. GeSn-based nanowire transistors[15]. These successes were enabled by the progress made in the GeSn epitaxy on Ge/ Si substrates[16,17] in industry-grade deposition reactors. Still, the thermal properties of GeSn alloys have not been explored yet, and their potential as CMOS-integrable TE materials remains unknown. The few existing experimental reports deal with amorphous or polycrystalline films[18,19] while, ideally, good thermoelectric materials should be crystalline, where phonon scattering occurs without disrupting the electrical conductivity[20].

In this work, the TE properties of high-quality GeSn epitaxial layers on Si are investigated. To this end, the GeSn lattice thermal conductivity κ_{latt} is first extracted via Raman thermometry and an extended analytical model of the heat transfer, adapted to the GeSn/Ge heterostructure. The extracted values of κ_{latt} are used to estimate the figure of merit ZT for different Sn content in the GeSn alloys. Our results show that GeSn alloys can be front-runners in the quest for TE materials in the low temperature range.

EXPERIMENTAL METHODS

$Ge_{1-x}Sn_x$ alloys were epitaxially grown on 1 µm-thick Ge buffers on 200 mm Si(100) wafers in an industry Chemical Vapor Deposition (CVD) reactor, using commercially-available digermane (Ge_2H_6) and tin-tetrachloride ($SnCl_4$) precursors. The epitaxy was performed at relatively low temperatures <400°C to avoid Sn segregation, and the Sn content, controlled by the growth temperature, was varied between 5 and 14at.%. Sn content was evaluated by Rutherford Backscattering Spectroscopy (RBS) and confirmed by X-Ray diffraction measurements. Details can be found elsewhere[17].

Table 1. Summary of the physical properties of the epitaxial GeSn alloys analyzed in this work.

Sample	Growth temperature (°C)	Sn content (at.%)	Thickness (nm)	In-plane strain at RT (%)	Raman position at RT (cm^{-1})	Thermal conductivity (W K^{-1} m^{-1})
Sn5	400	5	770	-0.13	297.0±0.1	18±3
Sn8	375	8.5	770	-0.2	294.6±0.1	10±1
Sn12_1	350	12.5	700	-0.32	291.1±0.1	5.2±0.3
Sn12_2	350	12	290	-0.62	291.2±0.2	4.0±0.2

Sn12_3	350	12	90	-1.5	298.3±0.1	4.3±0.5
Sn14	340	14	350	-0.55	293.5±0.1	3.7±0.2

The high epitaxial quality of the film can be observed in the high-resolution transmission electron microscopy image in **Figure 1**a.

The lattice parameters of the different GeSn alloys were measured via high-resolution x-ray diffraction (HR-XRD) as a function of temperature, as shown in Figure 1b-c. GeSn (004) and (224) Bragg reflections at various temperatures have been used to determine the in- and out-of-plane lattice constants ($a_{||}$ and $a_{\perp}$). The unstrained lattice constant (cubic GeSn structure) has been quantified using the biaxial strain model equation $a = (a_{\perp}+Pa_{||})/(1+P)$, $P = 2\upsilon/(1-\upsilon)$, where the Poisson´s ratio υ in the investigated stoichiometry range was assumed to be linear between υ_{Ge} = 0.273 and υ_{Sn} = 0.298, and independent on temperature. Thus, the temperature dependent lattice strain, $\varepsilon=(a_{||}-a)/a$, of the investigated samples is given in Figure 1d. The strain decreases with increasing temperature, following the linear relationship $\Delta\varepsilon \approx -3\cdot10^{-6}K^{-1}\ \Delta T$, due to the thermal expansion coefficient difference between GeSn, Ge, and the much thicker Si substrate[21].

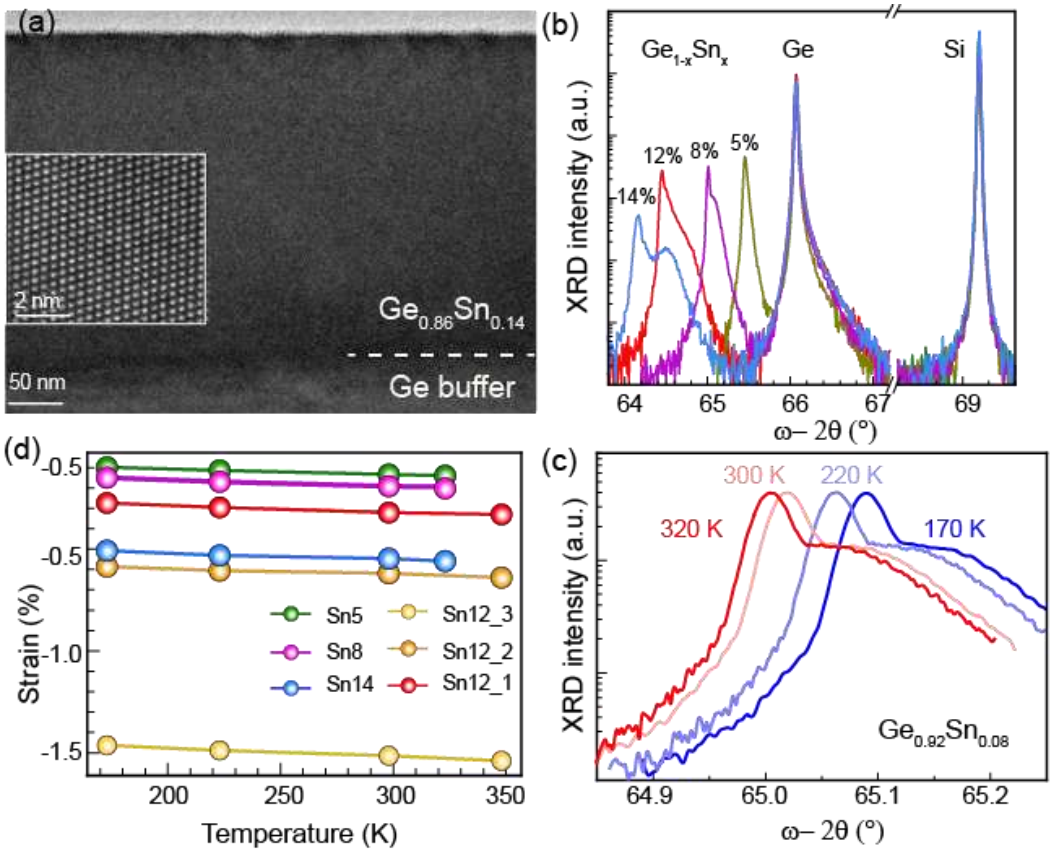

Figure 1. (a) XTEM micrograph of a $Ge_{0.86}Sn_{0.14}$/Ge heterostructure (sample S12_2) with high resolution TEM as inset. (b) XRD ω–2θ rocking curves for samples with different Sn content. (c) XRD ω–2θ rocking curves for Sn signal for sample Sn8. (d) XRD extracted strain values, ε, as a function of temperature for all investigated GeSn layers

For assessing the thermal conductivity, an experimental procedure based on Raman thermometry and a mathematical model was developed. Raman spectroscopy was performed using optical excitation at a wavelength $\lambda = 532$ nm (see Supporting Information, SI, and Figure S1), initially at a non-heating incident power density $P_0 < 25$ kW/cm^2, while the sample temperature is controlled by a cooling/heating stage.

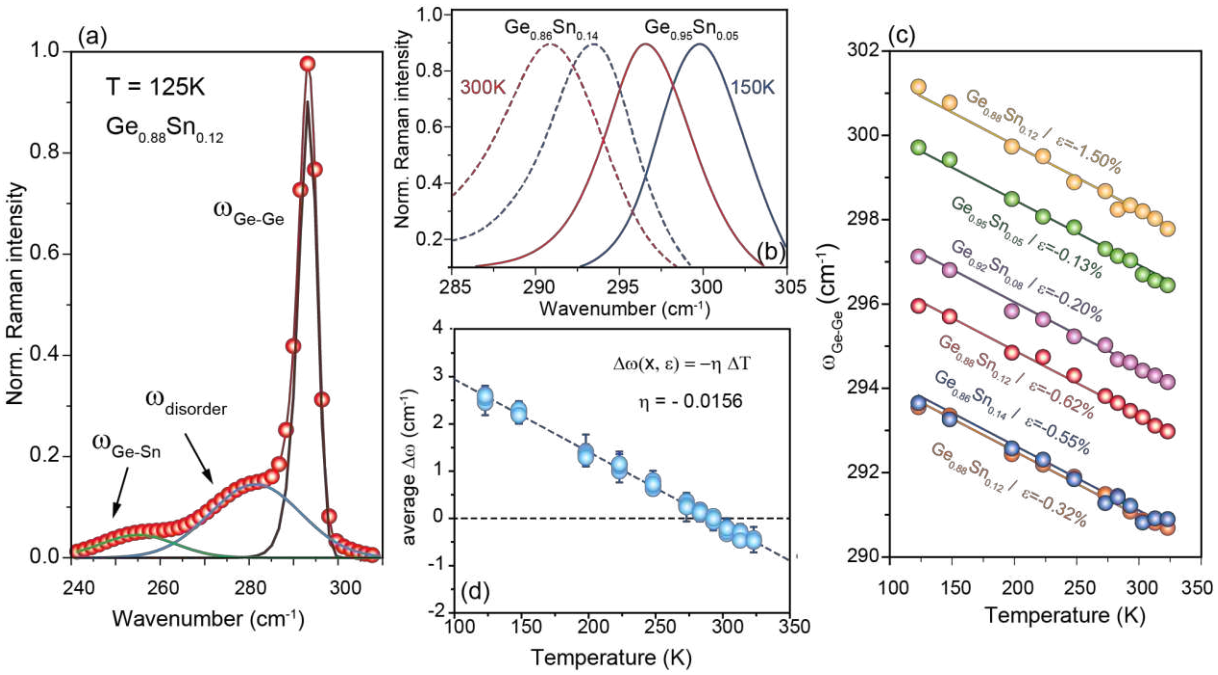

Figure 2. (a) Raman spectrum of a $Ge_{0.88}Sn_{0.12}$ alloy acquired at 125 K and mode fitting. (b) Normalized intensity of the $\omega_{Ge\text{-}Ge}$ Raman mode for $Ge_{0.95}Sn_{0.05}$ (full line) and $Ge_{0.86}Sn_{0.14}$ (dotted line) at temperatures of 150K (blue) and 300K (red). (c) The position of Ge-Ge Raman mode as a function of temperature, measured under 532 nm excitation with ~1 mW optical power. (d) The Ge-Ge mode shift relative to the value at 300K. The experimental points stand on the same line, Eq.1, with the slope of -0.0156 $cm^{-1}K^{-1}$ (dashed line).

A typical Raman spectrum, here for sample Sn12_1 at 125K, is shown in Figure 2a. It features: i) a main peak, $\omega_{Ge\text{-}Ge}$, at 295 cm^{-1}, corresponding to the Ge-Ge vibration mode in the Ge-Sn alloy, ii) a lower-intensity peak centered at $\omega_{Ge\text{-}Sn}$~258 cm^{-1}, corresponding to Ge-Sn vibration mode. The main peak has a tail extending on the low-energy side due to Sn disorder-induced Ge-Ge phonon scattering[22,23]. For consistency, an exponentially-modified Gaussian function was used for fitting of the peak position[24].

RESULTS AND DISCUSSION

Raman thermometry

The Raman thermometry calibration procedure is based on the temperature-dependence of the $\omega_{Ge\text{-}Ge}$ vibration mode position. As illustrated in Figure 2b for $Ge_{0.95}Sn_{0.05}$ and $Ge_{0.86}Sn_{0.14}$ alloys, the Raman spectrum red-shifts with temperature increasing from 125K to 325K. For each sample, the $\omega_{Ge\text{-}Ge}$ Raman peak energy decreases linearly, following the function $\omega(x,\varepsilon,T) = \omega_o(x,\varepsilon,T_0) + \eta(T - T_0)$ (see Figure 2c). While the value $\omega_0(x,\varepsilon,T_0)$ is sample-specific, the slope, with a mean value of $\eta = -0.0156 \pm 0.0002$ $cm^{-1}K^{-1}$, is the same for all samples. This is highlighted in Figure 2d, where the Raman shift, $\Delta\omega$, for T_0= 273K is plotted as:

$$\Delta\omega = \omega(x,\varepsilon,T) - \omega(x,\varepsilon,T_0) = \eta\Delta T \quad (1)$$

$$\Rightarrow \Delta T = \frac{\Delta\omega}{\eta} \ . \quad (2)$$

This implies that the temperature-induced shift of the Raman energy does not depend on either the Sn content or the value of the strain. The η value is close to that obtained in the Ge/Si system[25] and includes the effect of the thermal strain (Figure 1b) on the Raman shift. Note that Eq. (2), through the coefficient η, forms the Raman thermometry equation for GeSn/Ge alloys of any composition and strain.

Now, the thermal conductivity is addressed by employing the Raman set-up to simultaneously heat the sample and extract the local temperature. Using the experimental value of η, the temperature increase due to the laser heating (Figure 3a) is calculated from the shift of $\omega_{Ge\text{-}Ge}$ Raman mode as a function of P_{abs} (the absorbed power density), $\Delta\omega(P) = \omega(x, \varepsilon, P_{abs}, T_0) - \omega(x,\varepsilon, T_0,P_0)$. The quantity $P_{abs}= P_{inc}$ (1-R) is the fraction of the incident power (P_{inc}) absorbed in the

sample, where $R = 0.5$ is the sample reflectivity. Large Raman shifts obtained at laser powers where local melting occurs[21] have not been considered in the analysis (SI, Figure S1).

Although a linear increase of the sample temperature with increasing optical power is observed, the slope is Sn-content dependent.

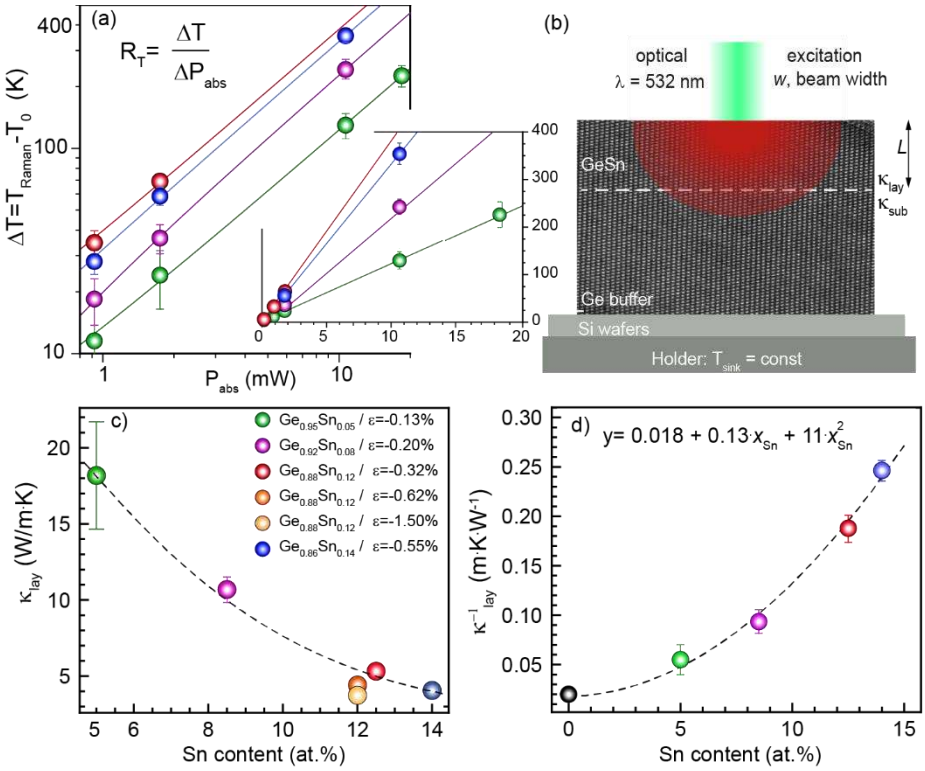

Figure 3. a) Temperature increase measured by Raman as a function of laser power, calculated as $\Delta\omega(P)/\eta$ in log-log plot and linear scale (inset). Solid lines show their trends in double logarithmic and linear scale. (b) Schematic view of the heat transport model described in the text, using a TEM image of the GeSn/Ge interface of sample Sn12_3. c) Thermal conductivity of GeSn layers, calculated via Eq. 4 in the text, as a function of Sn content. d) Inverse of the thermal conductivity (thermal resistivity) as a function of Sn content allows a simple fit of the experimental data: $0.018 + 0.13 \cdot x_{Sn} + 11 \cdot x_{Sn}^2$.

Thermal conductivity

To evaluate the GeSn layer total thermal conductivity κ, the analytical model of heat diffusion developed in Ref. [26] is extended to the case of a finite layer thickness, L, and thermal conductivity κ_{lay} on a semi-infinite substrate with thermal conductivity κ_{sub}, and considering a Gaussian distribution of the absorbed power density $\frac{P_{abs}}{2\,\pi w^2}\exp\left(-\frac{r^2}{2w^2}\right)$, where w is the beam radius and P_{abs} the absorbed light power (see Figure 3b and SI). The quasi-stationary temperature distribution in the GeSn/Ge heterostructure was analytically simulated following two independent procedures:

i) solving the stationary heat transport equation with appropriate boundary conditions using cylindrical coordinates and Hankel transform, similar to Ref. [26] for semi-infinite layer;

ii) considering the zero frequency limit of the matrix formalism developed for a time-domain heating problem in layered structures [27].

Method (ii) is powerful in its scalability to multilayer systems and frequency-dependent case. It is however interesting the use of method (i), whose derivation is given in SI, to obtain the full solution of the spatial dependence of the temperature (in the steady state). In particular, it is found for the layer and the substrate:

$$T_{lay}(r',z') = T_0 + T_c\int_0^\infty \frac{\exp(-xz') + u\exp(-2xl)\exp(xz')}{1-u\exp(-2xl)}\exp(-x^2/2)\,J_0(xr')dx \quad (3)$$

$$T_{sub}(r',z') = T_0 + T_c(1+u)\int_0^\infty \frac{\exp(-xz')}{1-u\exp(-2xl)}\exp(-x^2/2)\,J_0(xr')dx$$

where r', z' are the radius and depth scaled by w, and $T_c=P/(2\pi w\kappa_{lay})$, $u=\frac{\kappa_{lay}-\kappa_{sub}}{\kappa_{lay}+\kappa_{sub}}$, and l=L/w, T_0 is the temperature of the material at equilibrium prior to the laser heating. The $T_{lay}(r,z)$ function is valid in the top layer (z<L), while the $T_{sub}(r,z)$ is valid in the substrate (z>L).

Equation 3 gives the heat distribution in the GeSn/Ge heterostructure. As an example, a 90 nm-layer with κ_{lay}=4 W m^{-1} K on the top of Ge (κ_{sub}=60 W m^{-1} K) was considered to calculate the temperature distribution on the surface plane and in the vertical direction (Figure 4). The surface temperature follows the radial distribution of the incident beam (Figure 4a; in the vertical direction, the effect of different thermal conductivity of the two materials is seen by the change of the temperature gradient ("wave front") at the interface (Figure 4b). This plot highlights the effect of the conductivity mismatch on heat transport, especially for the case of thin layers such as those considered for optical and electronics applications. This is very relevant in Raman thermometry analysis, as discussed below.

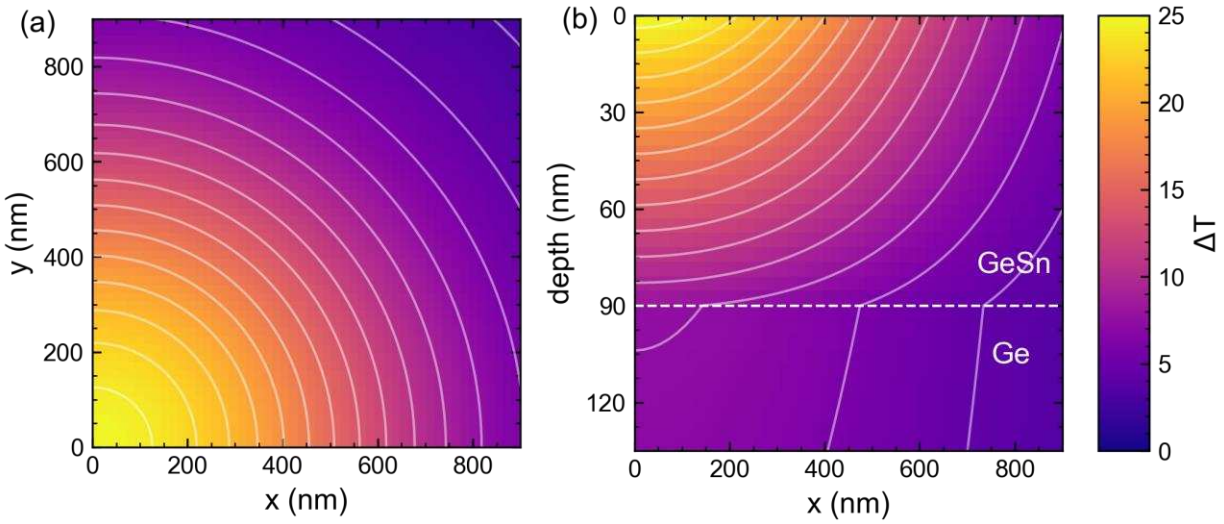

Figure 4. Calculated temperature increase for sample Sn12_3 (Sn: 12at.%, strain at RT -1.5%, thickness 90 nm, κ = 4 W K^{-1} m^{-1}), at 1 mW total absorbed power. (a) In-plane temperature profile at the sample surface. The laser spot center is at (x,y)= (0,0). (b) Cross-section temperature profile. The dashed line marks the interface between GeSn layer and the Ge substrate.

For the Raman thermometry case, an effective temperature T_{Raman} is measured, which is the result of the convolution of the temperature profile at the surface $T_{lay}(r,z=0)$ with the light intensity profile (see SI for details). This quantity is also the results of method (ii), and the two methods yield the same formula:

$$T_{Raman} = T_0 + P_{abs}\left[\frac{1}{2\pi w \kappa_{lay}} F\left(\frac{\kappa_{lay}-\kappa_{sub}}{\kappa_{lay}+\kappa_{sub}}, \frac{L}{w}\right)\right] \Longrightarrow \Delta T = \frac{\Delta\omega(P_{abs})}{\eta} \quad (4)$$
$$= R_T \Delta P_{abs},$$

$$F(u,l) = \int_0^\infty d\xi \frac{1+u\exp(-2l\xi)}{1-u\exp(-2l\xi)}\exp(-\xi^2) \quad (4.1)$$

Here, L is the thickness of the GeSn layer (Table 1), T_0 is the temperature of the material at equilibrium prior to the laser heating, κ_{sub}, and κ_{lay} are the thermal conductivities of Ge and GeSn layers, respectively. The expression in square brackets in Eq. 4 is the material "effective thermal resistance", R_T, and the auxiliary function $F(u,l)$ accounts for the effects of finite layer thickness and of thermal conductivity mismatch (SI Figure S2). For $L \rightarrow \infty$, or $\kappa_{sub} = \kappa_{lay}$, the result for one semi-infinite layer[26], $F(u,l) = \sqrt{\pi}/2$, is recovered.

The coefficient R_T is experimentally measured from the data in Figure 3a. The value for the Ge thermal conductivity, κ_{sub} = 56±6 W m^{-1} K^{-1} [26,28], was obtained on a Ge/Si sample using the semi-infinite layer model. Using this κ_{sub} value, the value of κ_{lay} is obtained by solving numerically the integral in Eq. 4.1. The extracted thermal conductivity for GeSn alloys, κ_{lay}, strongly decreases with the increase of Sn content (Figure 3c). However, for the same alloy, here $Ge_{0.88}Sn_{0.12}$, κ_{lay} does not show a clear dependence on material strain in the rather large range of compressive biaxial strains investigated (from -3.2×10^{-3} to -1.5×10^{-2}). Note that a larger epitaxial strain implies a lower degree of plastic relaxation of the GeSn/Ge heterostructure, which, in turn, is associated to a thinner epi-layer and to a lower density of threading and misfit dislocations. Additional investigations are necessary to disentangle the impact of these physical characteristics on the

thermal conductivity. The inverse of the thermal conductivity, $1/\kappa_{lay}$, as a function of Sn content, (Figure 3d), is well fitted by a quadratic expression $y = 0.018 + 0.13 \cdot x_{Sn} + 11 \cdot x_{Sn}^2$. This relation holds for the Sn content range up to 15 at.%. In principle, the measured κ_{lay} is the total thermal conductivity, comprising both the lattice, κ_{latt}, and electronic, κ_e, contributions, Nonetheless, owing to the low carrier density of $\sim 1\text{-}4\times10^{17}$cm^{-3} measured in our nominally intrinsic samples by electrochemical capacitance-voltage (ECV) profiling, the lattice thermal conductivity κ_{latt} largely dominates. The carrier density is not caused by reactor background or unintentional doping but is attributed to the presence of acceptor-like states induced by the misfit and threading dislocations at the GeSn/Ge interface responsible for the plastic relaxation of the GeSn layer.

The lack of TE data for GeSn crystalline materials makes it difficult to benchmark our findings against the literature. However, if we consider large-grain poly-crystalline $Ge_{0.95}Sn_{0.05}$ layers[18], a value of κ =18.6 W·m^{-1}·K^{-1} extracted by thermo-reflectance method was reported, very similar to the value obtained here for heteroepitaxial alloy of the same composition. For higher Sn composition, polycrystalline $Ge_{0.864}Sn_{0.136}$ alloy, the reported value κ =1 W·m^{-1}·K^{-1} [29] is lower than κ = 4.0 W·m^{-1}·K^{-1} obtained for crystalline $Ge_{0.86}Sn_{0.14}$. Extrapolating to GeSn alloys with Sn content of 20 at.%, using the empirical function from Figure 3, $\kappa_{latt} \sim 2.5$ W·m^{-1}·K^{-1} is obtained, comparable to 3 W·m^{-1}·K^{-1} given by numerical simulations in Ref. [30]. The values obtained here, based on the experimental lattice conductivity, are in excellent agreement with the theoretical estimations of Khatami and Aksamija[31]. For poli-Si values above 8 W·m^{-1}·K^{-1} are reported [32], and 5 W·m^{-1}·K^{-1} in SiGe superlattice by thickness and strain engineering [33]. In contrast to poli-Si,SiGe NWs or SiGe/Ge superlattices the excellent electrical performances of GeSn[15] makes the GeSn an attractive thermoelectric material, as discussed below.

Computation of thermoelectric performances

The experimental thermal conductivity values were used to evaluate the material thermoelectric efficiency.[34] The ZT was calculated for cubic structure (space group Fd-3m) GeSn alloys with Sn composition in the range of 0 - 20at.% in the temperature range 200 - 600K, and electron density, n_e, 5×10^{17} cm^{-3} - 5×10^{19} cm^{-3}. To get a realistic picture, our modelling includes a density of acceptor-like defects of $1\times10^{17}cm^{-3}$. As expected, in Figure 5a it can be observed that the ZT of the $Ge_{0.86}Sn_{0.14}$ alloy increases with the electron concentration, peaking at $\sim1.5\times10^{19}$ cm^{-3}. This behavior is observed for all GeSn alloys above 6at.%Sn. For larger n_e, the electron thermal conductivity, κ_{el}, becomes of the order of κ_{latt}, and, together with increased impurity scattering, this reduces the Seebeck coefficient and carrier mobility. Consequently, in total these factors decrease ZT. The $Ge_{0.86}Sn_{0.14}$ alloy has a respectable ZT ~0.4 around 300K and reaches an impressive ZT = 1.04 at 600K. For a better evaluation of the TE efficiency the maximum ZT, at $n_e=1.5\times10^{19}cm^{-3}$, is plotted as a function of alloy composition in Figure 5b. At all temperatures, the TE efficiency steeply increases up to about 14 at.% Sn, followed by a slow increase towards 20at% Sn, in accordance with the lattice thermal conductivity flattening at high Sn concentration.

Except for ZT, which determines the conversion efficiency, another important parameter for applications of thermoelectrics is the maximum power that can be generated, described by the power factor. Power factors of 75 – 80 $\mu W/cm\cdot K^2$ are obtained at RT and 110 – 120 $\mu W/cm\cdot K^2$ at 600K. The tradeoff between efficiency and power generation can be seen by plotting both parameters on the same electron concentration scale (Figure 5c), which shows that the efficiency and the generated power reach their maxima for different material parameters. $Ge_{0.88}Sn_{0.12}$ and $Ge_{0.86}Sn_{0.14}$ alloys offer the best balance for TE applications. Larger Sn content layers are not only

difficult for epitaxial growth, because it requires low processing temperatures (~250°C), but they also have lower power factor.

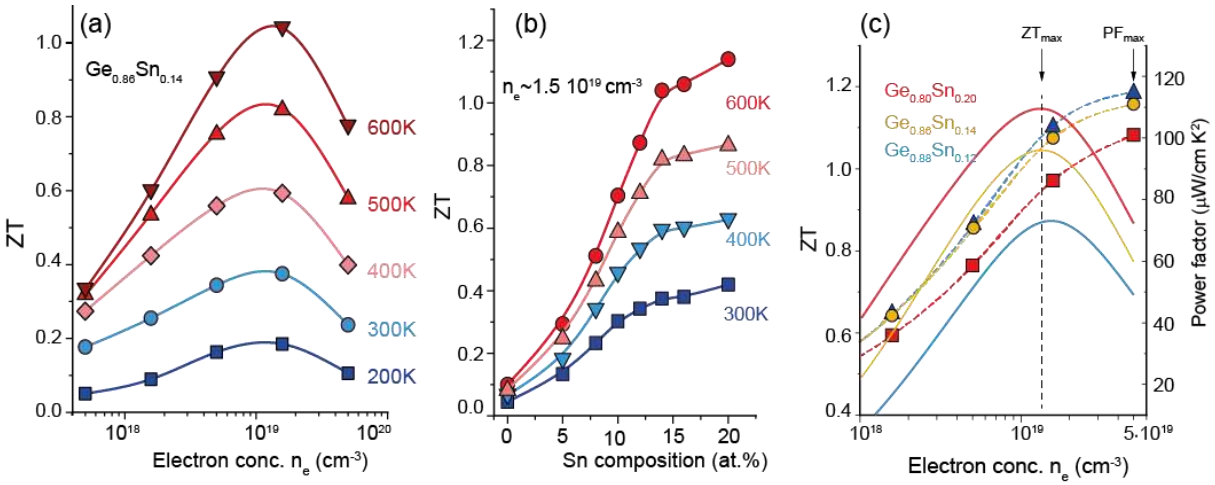

Figure 5. (a) Figure of merit ZT as a function of electron concentration for $Ge_{0.86}Sn_{0.14}$ alloy. (b) Calculated ZT at different temperatures for electron density $n_e = 1.5x10^{19}$ cm^{-3} for GeSn alloys with Sn content in the range 0-20at.%. (c) ZT (solid lines, left axis) and power factor (dashed lines, right axis) dependence on electron density for different GeSn alloys, at T=600 K.

The GeSn alloys considered here are benchmarked against the state-of-the-art RT thermoelectric materials (Figure 6)[35]. GeSn alloys are limited in operation temperature by the low epitaxial growth temperature to about 600K. While $Ge_{0.86}Sn_{0.14}$ alloys may reach ZT=1 at this temperature, their group IV alternative, $Si_{0.80}Ge_{0.20}$ alloy, has ZT~0.3 and a maximum ZT~1 at 900K[11]. Regarding the IV-VI chalcogenides, the fair comparison is between pristine crystalline materials. Both $Ge_{0.88}Sn_{0.12}$ and $Ge_{0.86}Sn_{0.14}$ alloys are outperforming PbTe, while for any Sn content GeSn shows a larger ZT than SnTe, GeTe and SnSe for temperatures up to 600K. However, all these materials show strongly enhanced TE performance above 700K, or by defect engineering or co-alloying,

reaching values up to ZT~2[7,36,37]. The state-of-the-art Bi_2Te_3 still has a larger ZT than $Ge_{0.86}Sn_{0.14}$ up to 450K, where GeSn becomes more efficient. Note, however, that group IV includes other semiconductor alloys, e.g. ternary SiGeSn alloys, that may offer an even better TE performance than GeSn. Using the theoretical data values for lattice thermal conductivity of 1.8 $W \cdot m^{-1} \cdot K^{-1}$ from Ref. [31] the $Si_{0.10}Ge_{0.78}Sn_{0.12}$ ternary alloy well outperforms the Bi_2Te_3 competitor. The highly crystalline epitaxial growth of such alloys was already demonstrated[38] but was not thoroughly investigated to date[39].

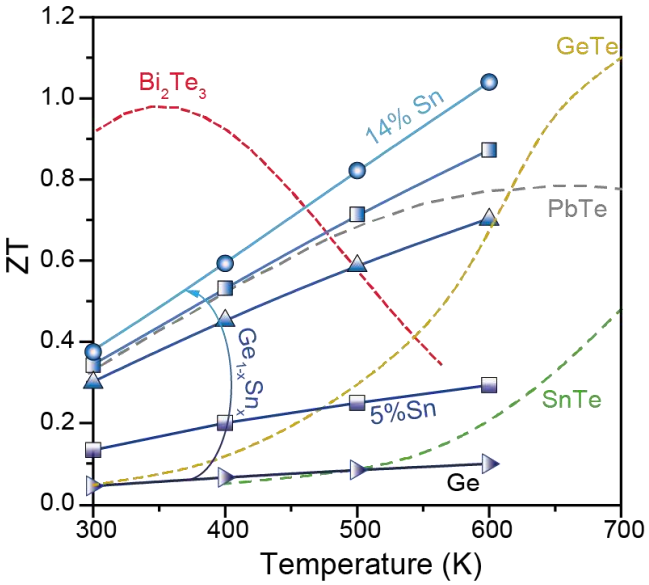

Figure 6. Benchmarking of ZT for GeSn alloys (this work) and BiTe, PbTe35, pristine SnTe7 and GeTe5 thermoelectric materials in the temperature range 300-600K.

CONCLUSION

In summary, we have shown that by alloying the semi-metal Sn with the technology-relevant Ge, the GeSn semiconductor alloy features very promising thermoelectric properties in the 300-600K temperature range. In particular, we have shown that the lattice thermal conductivity of GeSn alloys strongly decreases with the Sn content, reaching a low value $\kappa_{latt} \sim 4.0$ $W \cdot m^{-1} \cdot K^{-1}$ for

14 at.%Sn. Our modelling indicates that $Ge_{0.86}Sn_{0.14}$ alloy may offer a large thermoelectric figure of merit ZT=1.04. Even though a high-ZT device based on GeSn has yet to be demonstrated, the experimental data and the simulations presented here should stimulate a renewed interest in Group IV complex thermoelectric semiconductors. Being epitaxially grown on Si and CMOS-compatible, this system may be a very promising way to combine and monolithically integrate electronic, photonic and thermoelectric functions on one IC, a major push for autonomous systems.

ASSOCIATED CONTENT

Supporting Information. Experimental methods, additional information on Raman material characterization, theoretical modeling of heat transport and thermoelectric performance.

AUTHOR INFORMATION

Corresponding Author

*spirito@ihp-microelectronics.com. * d.m.buca@fz-juelich.de.

Author Contributions

The manuscript was written through contributions of all authors. All authors have given approval to the final version of the manuscript.

Notes

The authors declare no competing financial interest.

ACKNOWLEDGMENT

This research received funding for CVD growth investigations from Federal Ministry of Education and Research (BMBF) under ForMikro project “SiGeSn-NanoFETs”.

REFERENCES

(1) Haddad, C.; Périlhon, C.; Danlos, A.; François, M.-X.; Descombes, G. Some Efficient Solutions to Recover Low and Medium Waste Heat: Competitiveness of the Thermoacoustic Technology. *Energy Procedia* **2014**, *50*, 1056–1069. https://doi.org/10.1016/j.egypro.2014.06.125.

(2) Kim, C. S.; Yang, H. M.; Lee, J.; Lee, G. S.; Choi, H.; Kim, Y. J.; Lim, S. H.; Cho, S. H.; Cho, B. J. Self-Powered Wearable Electrocardiography Using a Wearable Thermoelectric Power Generator. *ACS Energy Lett.* **2018**, *3* (3), 501–507. https://doi.org/10.1021/acsenergylett.7b01237.

(3) Thermoelectric Module Market Worth US$ 1,713.9 Mn by 2027 - TMR https://www.transparencymarketresearch.com/thermoelectric-modules-market.html (accessed Mar 15, 2021).

(4) *ICT - Energy Concepts for Energy Efficiency and Sustainability*; Fagas, G., Gammaitoni, L., Gallagher, J. P., Paul, D. J., Eds.; IntechOpen, 2017. https://doi.org/10.5772/62522.

(5) Liu, W.-D.; Wang, D.-Z.; Liu, Q.; Zhou, W.; Shao, Z.; Chen, Z.-G. High-Performance GeTe-Based Thermoelectrics: From Materials to Devices. *Advanced Energy Materials* **2020**, *10* (19), 2000367. https://doi.org/10.1002/aenm.202000367.

(6) Cagnoni, M.; Führen, D.; Wuttig, M. Thermoelectric Performance of IV-VI Compounds with Octahedral-Like Coordination: A Chemical-Bonding Perspective. *Adv. Mater.* **2018**, *30* (33), 1801787. https://doi.org/10.1002/adma.201801787.

(7) Tang, J.; Gao, B.; Lin, S.; Wang, X.; Zhang, X.; Xiong, F.; Li, W.; Chen, Y.; Pei, Y. Manipulation of Solubility and Interstitial Defects for Improving Thermoelectric SnTe Alloys. *ACS Energy Lett.* **2018**, *3* (8), 1969–1974. https://doi.org/10.1021/acsenergylett.8b01098.

(8) Jin, M.; Chen, Z.; Tan, X.; Shao, H.; Liu, G.; Hu, H.; Xu, J.; Yu, B.; Shen, H.; Xu, J.; Jiang, H.; Pei, Y.; Jiang, J. Charge Transport in Thermoelectric SnSe Single Crystals. *ACS Energy Lett.* **2018**, *3* (3), 689–694. https://doi.org/10.1021/acsenergylett.7b01259.

(9) DiSalvo, F. J. Thermoelectric Cooling and Power Generation. *Science* **1999**, *285* (5428), 703–706. https://doi.org/10.1126/science.285.5428.703.

(10) Mao, J.; Zhu, H.; Ding, Z.; Liu, Z.; Gamage, G. A.; Chen, G.; Ren, Z. High Thermoelectric Cooling Performance of N-Type $Mg_3 Bi_2$ -Based Materials. *Science* **2019**, *365* (6452), 495–498. https://doi.org/10.1126/science.aax7792.

(11) *CRC Handbook of Thermoelectrics*; Rowe, D. M., Ed.; CRC Press: Boca Raton, FL, 1995.

(12) Stange, D.; von den Driesch, N.; Zabel, T.; Armand-Pilon, F.; Rainko, D.; Marzban, B.; Zaumseil, P.; Hartmann, J.-M.; Ikonic, Z.; Capellini, G.; Mantl, S.; Sigg, H.; Witzens, J.; Grützmacher, D.; Buca, D. GeSn/SiGeSn Heterostructure and Multi Quantum Well Lasers. *ACS Photonics* **2018**, *5* (11), 4628–4636. https://doi.org/10.1021/acsphotonics.8b01116.

(13) Zhou, Y.; Miao, Y.; Ojo, S.; Tran, H.; Abernathy, G.; Grant, J. M.; Amoah, S.; Salamo, G.; Du, W.; Liu, J.; Margetis, J.; Tolle, J.; Zhang, Y.; Sun, G.; Soref, R. A.; Li, B.; Yu, S.-Q. Electrically Injected GeSn Lasers on Si Operating up to 100 K. *Optica, OPTICA* **2020**, *7* (8), 924–928. https://doi.org/10.1364/OPTICA.395687.

(14) Elbaz, A.; Buca, D.; von den Driesch, N.; Pantzas, K.; Patriarche, G.; Zerounian, N.; Herth, E.; Checoury, X.; Sauvage, S.; Sagnes, I.; Foti, A.; Ossikovski, R.; Hartmann, J.-M.; Boeuf, F.; Ikonic, Z.; Boucaud, P.; Grützmacher, D.; El Kurdi, M. Ultra-Low-Threshold Continuous-Wave and Pulsed Lasing in Tensile-Strained GeSn Alloys. *Nat. Photonics* **2020**. https://doi.org/10.1038/s41566-020-0601-5.

(15) Liu, M.; Yang, D.; Shkurmanov, A.; Bae, J. H.; Schlykow, V.; Hartmann, J.-M.; Ikonic, Z.; Baerwolf, F.; Costina, I.; Mai, A.; Knoch, J.; Grützmacher, D.; Buca, D.; Zhao, Q.-T. Epitaxial GeSn/Ge Vertical Nanowires for p-Type Field-Effect Transistors with Enhanced Performance. *ACS Appl. Nano Mater.* **2021**, *4* (1), 94–101. https://doi.org/10.1021/acsanm.0c02368.

(16) Dou, W.; Benamara, M.; Mosleh, A.; Margetis, J.; Grant, P.; Zhou, Y.; Al-Kabi, S.; Du, W.; Tolle, J.; Li, B.; Mortazavi, M.; Yu, S.-Q. Investigation of GeSn Strain Relaxation and Spontaneous Composition Gradient for Low-Defect and High-Sn Alloy Growth. *Sci Rep* **2018**, *8* (1), 5640. https://doi.org/10.1038/s41598-018-24018-6.

(17) von den Driesch, N.; Stange, D.; Wirths, S.; Mussler, G.; Holländer, B.; Ikonic, Z.; Hartmann, J. M.; Stoica, T.; Mantl, S.; Grützmacher, D.; Buca, D. Direct Bandgap Group IV Epitaxy on Si for Laser Applications. *Chem. Mater.* **2015**, *27* (13), 4693–4702. https://doi.org/10.1021/acs.chemmater.5b01327.

(18) Uchida, N.; Hattori, J.; Lieten, R. R.; Ohishi, Y.; Takase, R.; Ishimaru, M.; Fukuda, K.; Maeda, T.; Locquet, J.-P. Carrier and Heat Transport Properties of Poly-Crystalline GeSn Films for Thin-Film Transistor Applications. *Journal of Applied Physics* **2019**, *126* (14), 145105. https://doi.org/10.1063/1.5085470.

(19) Utsumi, J.; Ishimaru, T.; Hayakawa, Y.; Shimura, Y. Reduced Thermal Conductivity of a Ge1-XSnx Layer Formed on a Self-Assembled Sn Nanodot Template. *Semicond. Sci. Technol.* **2018**, *33* (12), 124004. https://doi.org/10.1088/1361-6641/aadc00.

(20) Jana, M. K.; Biswas, K. Crystalline Solids with Intrinsically Low Lattice Thermal Conductivity for Thermoelectric Energy Conversion. *ACS Energy Lett.* **2018**, *3* (6), 1315–1324. https://doi.org/10.1021/acsenergylett.8b00435.

(21) Zaumseil, P.; Hou, Y.; Schubert, M. A.; von den Driesch, N.; Stange, D.; Rainko, D.; Virgilio, M.; Buca, D.; Capellini, G. The Thermal Stability of Epitaxial GeSn Layers. *APL Materials* **2018**, *6* (7), 076108. https://doi.org/10.1063/1.5036728.

(22) Slav, A.; Dascalescu, I.; Lepadatu, A.-M.; Palade, C.; Zoita, N. C.; Stroescu, H.; Iftimie, S.; Lazanu, S.; Gartner, M.; Buca, D.; Teodorescu, V. S.; Ciurea, M. L.; Braic, M.; Stoica, T. GeSn/SiO_2 Multilayers by Magnetron Sputtering Deposition for Short-Wave Infrared Photonics. *ACS Appl. Mater. Interfaces* **2020**, *12* (50), 56161–56171. https://doi.org/10.1021/acsami.0c15887.

(23) Liu, T.; Miao, Y.; Wang, L.; Zhu, G.; Hu, H.; Zhong, Z.; Yang, X.; Jiang, Z. Temperature Dependence of Raman Scattering in GeSn Films. *Journal of Raman Spectroscopy* **2020**, *51* (7), 1092–1099. https://doi.org/10.1002/jrs.5874.

(24) D'Costa, V. R.; Tolle, J.; Roucka, R.; Poweleit, C. D.; Kouvetakis, J.; Menéndez, J. Raman Scattering in $Ge_{1-y}Sn_y$ Alloys. *Solid State Communications* **2007**, *144* (5), 240–244. https://doi.org/10.1016/j.ssc.2007.08.020.

(25) Manganelli, C. L.; Virgilio, M.; Skibitzki, O.; Salvalaglio, M.; Spirito, D.; Zaumseil, P.; Yamamoto, Y.; Montanari, M.; Klesse, W. M.; Capellini, G. Temperature Dependence of Strain–Phonon Coefficient in Epitaxial Ge/Si(001): A Comprehensive Analysis. *Journal of Raman Spectroscopy* **2020**, *51* (6), 989–996. https://doi.org/10.1002/jrs.5860.

(26) Stoib, B.; Filser, S.; Stötzel, J.; Greppmair, A.; Petermann, N.; Wiggers, H.; Schierning, G.; Stutzmann, M.; Brandt, M. S. Spatially Resolved Determination of Thermal Conductivity by Raman Spectroscopy. *Semicond. Sci. Technol.* **2014**, *29* (12), 124005. https://doi.org/10.1088/0268-1242/29/12/124005.

(27) Cahill, D. G. Analysis of Heat Flow in Layered Structures for Time-Domain Thermoreflectance. *Review of Scientific Instruments* **2004**, *75* (12), 5119–5122. https://doi.org/10.1063/1.1819431.

(28) Glassbrenner, C. J.; Slack, G. A. Thermal Conductivity of Silicon and Germanium from 3°K to the Melting Point. *Phys. Rev.* **1964**, *134* (4A), A1058–A1069. https://doi.org/10.1103/PhysRev.134.A1058.

(29) Uchida, N.; Maeda, T.; Lieten, R. R.; Okajima, S.; Ohishi, Y.; Takase, R.; Ishimaru, M.; Locquet, J.-P. Carrier and Heat Transport Properties of Polycrystalline GeSn Films on SiO_2. *Appl. Phys. Lett.* **2015**, *107* (23), 232105. https://doi.org/10.1063/1.4937386.

(30) Lee, Y.; Hwang, G. S. Molecular Dynamics Investigation of the Thermal Conductivity of Ternary Silicon–Germanium–Tin Alloys. *J. Phys. D: Appl. Phys.* **2017**, *50* (49), 494001. https://doi.org/10.1088/1361-6463/aa94a0.

(31) Khatami, S. N.; Aksamija, Z. Lattice Thermal Conductivity of the Binary and Ternary Group-IV Alloys Si-Sn, Ge-Sn, and Si-Ge-Sn. *Phys. Rev. Applied* **2016**, *6* (1), 014015. https://doi.org/10.1103/PhysRevApplied.6.014015.

(32) Takeuchi, H.; Yokogawa, R.; Takahashi, K.; Komori, K.; Morimoto, T.; Yamashita, Y.; Sawamoto, N.; Ogura, A. Thermal Conductivity Characteristics in Polycrystalline Silicon with Different Average Sizes of Grain and Nanostructures in the Grains by UV Raman Spectroscopy. *Jpn. J. Appl. Phys.* **2020**, *59* (7), 075501. https://doi.org/10.35848/1347-4065/ab9624.

(33) Huxtable, S. T.; Abramson, A. R.; Tien, C.-L.; Majumdar, A.; LaBounty, C.; Fan, X.; Zeng, G.; Bowers, J. E.; Shakouri, A.; Croke, E. T. Thermal Conductivity of Si/SiGe and SiGe/SiGe Superlattices. *Appl. Phys. Lett.* **2002**, *80* (10), 1737–1739. https://doi.org/10.1063/1.1455693.

(34) Narducci, D. Do We Really Need High Thermoelectric Figures of Merit? A Critical Appraisal to the Power Conversion Efficiency of Thermoelectric Materials. *Appl. Phys. Lett.* **2011**, *99* (10), 102104. https://doi.org/10.1063/1.3634018.

(35) Snyder, G. J.; Toberer, E. S. Complex Thermoelectric Materials. *Nature Mater* **2008**, *7* (2), 105–114. https://doi.org/10.1038/nmat2090.

(36) Roychowdhury, S.; Biswas, R. K.; Dutta, M.; Pati, S. K.; Biswas, K. Phonon Localization and Entropy-Driven Point Defects Lead to Ultralow Thermal Conductivity and Enhanced Thermoelectric Performance in $(SnTe)_{1-2x}(SnSe)_x(SnS)_x$. *ACS Energy Lett.* **2019**, *4* (7), 1658–1662. https://doi.org/10.1021/acsenergylett.9b01093.

(37) Moshwan, R.; Shi, X.-L.; Liu, W.-D.; Wang, Y.; Xu, S.; Zou, J.; Chen, Z.-G. Enhancing Thermoelectric Properties of InTe Nanoprecipitate-Embedded $Sn_{1-x}In_xTe$ Microcrystals through

Anharmonicity and Strain Engineering. *ACS Applied Energy Materials* **2019**. https://doi.org/10.1021/acsaem.9b00399.

(38) von den Driesch, N.; Stange, D.; Wirths, S.; Rainko, D.; Povstugar, I.; Savenko, A.; Breuer, U.; Geiger, R.; Sigg, H.; Ikonic, Z.; Hartmann, J.-M.; Grützmacher, D.; Mantl, S.; Buca, D. SiGeSn Ternaries for Efficient Group IV Heterostructure Light Emitters. *Small* **2017**, *13* (16), 1603321. https://doi.org/10.1002/smll.201603321.

(39) Peng, Y.; Miao, L.; Gao, J.; Liu, C.; Kurosawa, M.; Nakatsuka, O.; Zaima, S. Realizing High Thermoelectric Performance at Ambient Temperature by Ternary Alloying in Polycrystalline $Si_{1-x-y}Ge_xSn_y$ Thin Films with Boron Ion Implantation. *Sci Rep* **2019**, *9* (1), 14342. https://doi.org/10.1038/s41598-019-50754-4.

TOC GRAPHICS

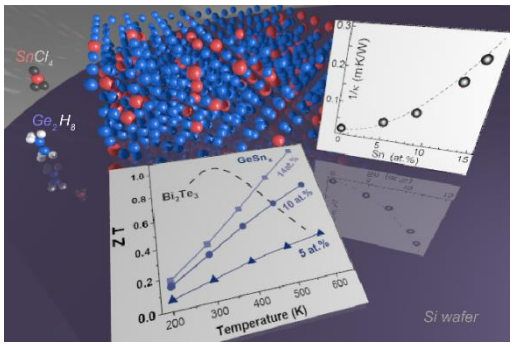

Supplementary information

Thermoelectric Efficiency of Epitaxial GeSn Alloys for Integrated Si-based Applications - Assessing the Lattice Thermal Conductivity by Raman Thermometry

Davide Spirito[1], Nils von den Driesch[2], Costanza Lucia Manganelli[1], Marvin Hartwig Zoellner[1], Agnieszka Anna Wiciak[1], Zoran Ikonic[3], Toma Stoica[4], Detlev Grützmacher[2], Dan Buca[2*] and Giovanni Capellini[1,5]*

[1]IHP – Leibniz-Institut für innovative Mikroelektronik, Im Technologiepark 25, 15236 Frankfurt (Oder), Germany

[2]Peter Grünberg Institute 9 (PGI-9) and JARA-Fundamentals of Future Information Technologies (JARA-FIT), Forschungszentrum Jülich, 52425 Jülich, Germany

[3]Pollard Institute, School of Electronic and Electrical Engineering, University of Leeds, Leeds LS2 9JT, UK

[4]National Institute of Materials Physics, 405A Atomistilor St., 077125 Magurele, Romania.

[5]Dipartimento di Scienze, Università Roma Tre, V.le G. Marconi 446, 00146 Roma, Italy.

**corresponding authors: spirito@ihp-microelectronics.com, d.m.buca@fz-juelich.de*

Table of content:

3. Modelling of thermal transport
4. TE parameters modelling

1. Methods

Raman spectroscopy. A Renishaw inVia system was used, equipped with HeNe laser at 633 nm and 532 nm diode lasers; using a grating with 1800 grooves/mm. A Linkam liquid-nitrogen cryostat was used to control the temperature of the sample in the range 98-323 K. A long working distance objective (50x, 0.5 NA) was used. The spot size (the waist, assuming a Gaussian profile) was estimated to be 900±10 nm measuring the intensity of the Raman peak of Si across a partially metallized Si chip. The laser power at the sample was measured with a Thorlabs PM16-130 calibrated power meter at the output of the objective.

XRD. Temperature dependent HR-XRD measurements have been conducted with a Rikagu Smart-Lab equipped with a 9 kW Cu rotating anode in line-focus geometry ($\lambda_{K\alpha}$ = 0.15406 nm). For the optical setup, a parabolic multilayer mirror, 2-bounce Ge(400) monochromator and 2-bounce Ge(220) analyzer crystal have been used. The sample environment was adjusted with a DCS 350 cooling stage enabling vacuum below 10^{-1} mbar and temperatures down to -100°C.

2. Raman spectrometry

The Raman spectrum is temperature dependent. The energy of the Raman $\omega_{Ge\text{-}Ge}$ vibration mode shift with the temperature is presented for two cases: i) the sample temperature is controlled through a cooling/heating stage (Fig S2a); ii) the sample is heated by optical excitation (Fig S2b). In the latter case, when the optical power exceeds a critical power, melting occurs and a large shift is observed. This spectra were not used in the calculation of the thermal conductivity.

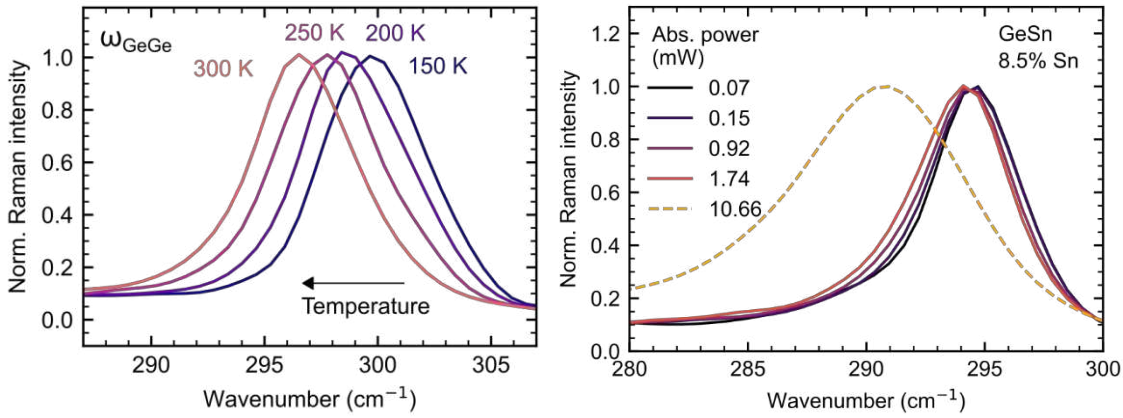

Figure S1: (a) Comparison of Raman $\omega_{Ge\text{-}Ge}$ vibration spectra for a GeSn layer with 5 at.%Sn. (b) Raman $\omega_{Ge\text{-}Ge}$ vibration spectra for a GeSn layer with 8.5 at.% Sn content at different absorbed power. At 10.66 mW (dashed line) damages were observed on the sample: the analysis of power dependence in the main text does not consider spectra acquired at this power.

3. Modelling of thermal transport

As described in the main text, the use of Raman thermometry to calculate the thermal conductivity of a sample requires the solution of heat diffusion equation in a geometry defined by the sample, and by the shape of the beam that provides the heat flux. Then, the solution for the temperature at the surface of the sample has to be considered and averaged within the probe beam to obtain the "Raman temperature" that is given by the shift in the spectral features.

The common case of a thin layer grown on top of a substrate with different thermal conductivity, which was studied in this work, is different from the simple case of a semi-infinite layer.

Below we give the details of the solution for the heat transport equation using the two methods described in the main text: i) a matrix formalism for heat flow, ii) solving the stationary heat transport equation with appropriate boundary conditions.

Raman temperature in 2-layer system: matrix formalism

The 2-layer case can be addressed in a general formalism for multi-layer samples using the matrix method[1], including frequency modulated heating.

Below, we summarize and use this method to derive Equation 3 in the main text.

The incoming laser beam, which provides both heating and temperature measurements via Raman spectroscopy, has the total power *P* and Gaussian profile at the surface of the sample of the form

$$H(r) = \frac{P_{abs}}{2\,\pi w^2} \exp\left(-\frac{r^2}{2w^2}\right) \tag{A1}$$

Because of the small penetration depth of the 532nm laser light used in this work, we approximate that the heating takes place at the film surface only. In the following, we consider P_{abs} as the absorbed power at the surface.Using the Hankel transform method with a frequency domain kernel, and assuming a "probe beam" of the same profile as the incoming power, the solution is given by the integral

$$\Delta T = 2\pi P_{abs} \int_0^\infty G(x) \exp(-4\pi^2 x^2 w^2)\, x dx \tag{A2}$$

where *G(x)* has to be calculated for the layer stack. To this aim, the amplitudes *B* describe the heat flow in positive and negative *z* directions (*z* being negative towards the substrate).

In the case of one layer of thickness L (labelled as *lay*) on the top of a semi-infinite substrate (*sub*), the formula reads

$$\begin{pmatrix} B_{lay}^{+} \\ B_{lay}^{-} \end{pmatrix} \tag{A3}$$
$$= \frac{1}{2\gamma_{lay}} \begin{pmatrix} \exp(-uv_{lay}L) & 0 \\ 0 & \exp(+v_{lay}L) \end{pmatrix} \begin{pmatrix} \gamma_{lay}+\gamma_{sub} & \gamma_{lay}-\gamma_{sub} \\ \gamma_{lay}-\gamma_{sub} & \gamma_{lay}+\gamma_{sub} \end{pmatrix} \begin{pmatrix} B_{sub}^{+} \\ B_{sub}^{-} \end{pmatrix}$$

with

$$v_i = \sqrt{4\pi^2 x^2 + q_i^2}\,,\ q_i^2 = i\omega/D_i, \gamma_i = v_i \kappa_i$$

In this frequency-dependent formalism, the low-frequency limit is given by D/w^2, where *D* is the thermal diffusivity; equivalently, this condition can be read so that the system response is steady

after a time of $\tau \sim 2\pi w^2/D$. In the case of Ge, $D \sim 35$ mm^2/s, and $\tau \sim 10^{-7}$ s. In measurements presented in the main text, the integration time is several tens of seconds, thus we can safely assume it to be in steady state, and we set $\omega=0$ in the above equations.

For the substrate, we can write $B_{sub}^{+} = 0, B_{sub}^{-} = 1$, and finally

$$\begin{pmatrix} B_{lay}^{+} \\ B_{lay}^{-} \end{pmatrix} = \frac{1}{2\kappa_{lay}} \begin{pmatrix} (\kappa_{lay} - \kappa_{sub})\exp(-2\pi x L) \\ (\kappa_{lay} + \kappa_{sub})\exp(+2\pi x L) \end{pmatrix}$$

so that

$$G(x) = \frac{1}{\gamma_{lay}} \frac{B_{lay}^{-} + B_{lay}^{+}}{B_{lay}^{-} - B_{lay}^{+}} \tag{A4}$$

$$= \frac{1}{2\pi x \kappa_{lay}} \frac{-(\kappa_{lay} - \kappa_{sub}) - (\kappa_{lay} + \kappa_{sub})\exp(4\pi x L)}{(\kappa_{lay} - \kappa_{sub}) - (\kappa_{lay} + \kappa_{sub})\exp(4\pi x L)}$$

$$= \frac{1}{2\pi x \kappa_{lay}} \frac{1 + u\exp(-4\pi x L)}{1 - u\exp(-4\pi x L)}$$

with $u = \frac{(\kappa_{lay} - \kappa_{sub})}{(\kappa_{lay} + \kappa_{sub})}$

Then the temperature is

$$\Delta T = P_{abs} \int_0^{\infty} \frac{1}{\kappa_{lay}} \frac{1 + u\exp(-4\pi x L)}{1 - u\exp(-4\pi x L)} \exp(-4\pi^2 x^2 w^2)\, dx \tag{A5}$$

and the integral is the "effective thermal resistance" measured by Raman thermometry. It can be re-written with the unitless $l=L/w$ as

$$\frac{\Delta T}{P_{abs}} = \frac{1}{2\pi\kappa_{lay} w} \int_0^{\infty} \frac{1 + u\exp(-2xl)}{1 - u\exp(-2xl)} \exp(-x^2)\, dx = \frac{1}{2\pi\kappa_{lay} w} F(u, l) \tag{A5}$$

$$F(u, l) = \int_0^{\infty} d\xi \frac{1 + u\exp(-2l\xi)}{1 - u\exp(-2l\xi)} \exp(-\xi^2)$$

This formalism can include an interface thermal resistance that can be modeled with a layer of finite conductivity and zero thickness. In this case, the calculation finds that, in the DC limit (steady-state), the interface layer does not appear in the final formula, thus justifying our approximation that there is no interface effect on the Raman temperature (however, the interface is relevant in time- or frequency-dependent measurements).

Raman temperature in 2-layer system: full solution of the heat equation

The equation to be solved, in cylindrical coordinates, is:

$$\frac{\partial^2 T_i}{\partial r^2} + \frac{1}{r}\frac{\partial T_i}{\partial r} + \frac{\partial^2 T_i}{\partial z^2} = 0 \qquad \text{(A6)}$$

to be solved in layer *i=sub* and *lay*. The surface is at *z=0* and (differently from the matrix method) z increases towards the substrate. The variable T is here the temperature difference from the temperature infinitely deep in the substrate.

As discussed before, we assume steady-state and ignore the transients.

The boundary conditions are:

BC1: At *z=0*: $-\kappa_{lay}\partial_z T_{lay}(r, z=0) = H(r)$

BC2: At z=L: $T_{lay}(r, z=L) = T_{sub}(r, z=L)$

BC3: At z=L: $-\kappa_{lay}\partial_z T_{lay}(r, z=L) = -\kappa_{sub}\partial_z T_{sub}(r, z=L)$

We search for a solution in terms of a weighted integral of basis functions given by an exponential part in z and Bessel function in r (this corresponds to the use of the Hankel transform). In particular:

$$T_{lay}(r,z) = \int_0^\infty (\mathrm{e}^{-\lambda z} + g(\lambda)\mathrm{e}^{+\lambda z}) J_0(\lambda r) f_{lay}(\lambda) d\lambda \qquad \text{(A7)}$$

and for layer 0:

$$T_{sub}(r,z) = \int_0^\infty (\mathrm{e}^{-\lambda z}) J_0(\lambda r) f_{sub}(\lambda) d\lambda \qquad \text{(A8)}$$

Here, λ (that is the eigenvalue for the operator) acts as a dummy variable in the integral, and $f_i(\lambda)$ is chosen according to the boundary conditions. $g(\lambda)$ weights the exponential that is increasing in z.

From the BC 1, and using an integral relations for Bessel and Gaussian functions, one finds

$$f_{lay}(\lambda)(1-g(\lambda)) = \frac{P_{abs}}{2\,\pi\kappa_{lay}}\exp\left(-\frac{w^2\lambda^2}{2}\right)$$

BC 2 gives

$$f_{lay}(\lambda)\left(\mathrm{e}^{-\lambda L} + g(\lambda)\mathrm{e}^{+\lambda L}\right) = f_{sub}(\lambda)\mathrm{e}^{-\lambda L}$$

and finally from BC 3

$$g(\lambda) = \mathrm{e}^{-2\lambda L}\frac{\kappa_{lay}-\kappa_{sub}}{\kappa_{lay}+\kappa_{sub}}$$

It is apparent that $g(\lambda)$ goes to 0 in the limit of infinite *L* or of equal thermal conductivities.

From these relation $f_{sub}(\lambda)$ and $f_{lay}(\lambda)$ can be derived. Using the above equation, the temperature of the two layers can be obtained by numerical integration.

To find the "Raman temperature" at the surface, only the solution at z=0 is needed. This simplifies the calculation, and using the integral form for the top layer we find:

$$T_{surface}(r) = T_{lay}(r, z=0) = \frac{P_{abs}}{2\,\pi\kappa_{lay}}\int_0^\infty \frac{1+g(\lambda)}{1-g(\lambda)}J_0(\lambda r)\exp\left(-\frac{w^2\lambda^2}{2}\right)d\lambda \qquad \text{(A9)}$$

The temperature measured by Raman is then the result of the overlap of this temperature and the light intensity profile, given by the integral

$$T_{Raman} = T_0 + \frac{1}{P}\int_0^{2\pi} d\phi \int_0^\infty T_{surface}(r)H(r)r\,dr$$

with T_0 being the temperature of the sample at infinity. The equation can be written, after simplification of constants

$$T_{Raman} = T_0 + \frac{P}{2\pi w\kappa_{lay}}F\left(\frac{\kappa_{lay}-\kappa_{sub}}{\kappa_{lay}+\kappa_{sub}}, \frac{L}{w}\right), \qquad \text{(A10)}$$

$$F(u,l) = \iint_{0,0}^{\infty,\infty} d\rho d\xi\ \rho J_0(\alpha\rho)\exp\left(-\frac{\xi^2+\rho^2}{2}\right)\frac{1+u\exp(-2l\xi)}{1-u\exp(-2l\xi)}$$

$$= \int_0^\infty d\xi\,\frac{1+u\exp(-2l\xi)}{1-u\exp(-2l\xi)}\exp(-\xi^2)$$

thus re-deriving the previous equation.

The spatial distribution of the temperature increase can be written, using the previous equations, as

$$T_{lay}(r',z') = T_c \int_0^{\infty} \frac{\exp(-xz') + u\exp(-2xl)\exp(xz')}{1-u\exp(-2xl)} \exp(-x^2/2) J_0(xr')dx \qquad \text{(A11)}$$

$$T_{sub}(r',z') = T_c(1+u) \int_0^{\infty} \frac{\exp(-xz')}{1-u\exp(-2xl)} \exp(-x^2/2) J_0(xr')dx$$

where r', z' are the radius and depth scaled by w, and $T_c = P/(2\pi w \kappa_{lay})$.

Analysis of the solution

In the case of single semi-infinite layer ($L/w \gg 1$), $F(u,l) = \sqrt{\pi}/2$.[2]

The integral function in eq. (A6) can be calculated numerically. In Figure S3a we show the dependence of $(T_{Raman}-T_0)/T_0$ as a function of L, using unitless parameters L/w, $\kappa_{lay}/\kappa_{sub}$, and P in units of ($\kappa_{sub} w T_0$) fixed at 1. Dotted and dashed lines in the Figure S3 show the limiting values calculated for a semi-infinite layer.

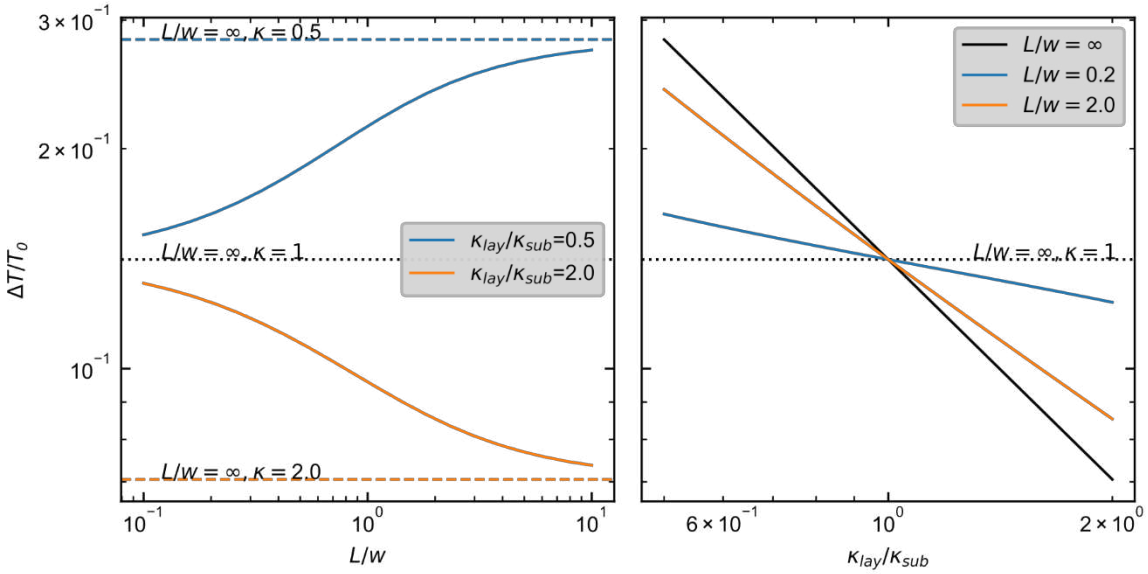

Figure S2: Effect of laser heating calculated using eq. A5/A10, displayed as relative increase in respect to T_0. a) Dependence on unitless layer thickness L/w, for different relative thermal conductivity $\kappa_{lay}/\kappa_{sub}$; dotted and dashed lines are calculated using the semi-infinite model. b) Dependence on the relative thermal conductivity $\kappa_{lay}/\kappa_{sub}$ for different unitless layer thickness L/w.

Several limit cases can be considered to validate this model.

- $L/w \to 0$: The temperature increase of a semi-infinite layer with $\kappa=\kappa_{sub}$ is expected (as interface effect should not be visible). The value is verified from formulas and by numerical integration.
- $L/w \to \infty$: the temperature increase of a semi-infinite layer with $\kappa=\kappa_{lay}$ is expected. This is verified as $g(\lambda) \to 0$, as well as by the numerical integration.
- $\kappa_{lay}=\kappa_{sub}$ ($u=0$): the temperature increase of a semi-infinite layer (with $\kappa=\kappa_{lay}=\kappa_{sub}$) is expected, and verified as $g(\lambda) \to 0$.
- $\kappa_{lay}/\kappa_{sub} \to 0$ ($u \to -1$): non-conductive top-layer, or highly conductive substrate: The temperature increase is expected to be higher than for a bare substrate with $\kappa=\kappa_{sub}$. This is verified by numerical integration.
- $\kappa_{lay}/\kappa_{sub} \to \infty$ ($u \to +1$): highly conductive top-layer: the heat is efficiently conducted to the substrate, so the temperature increase is expected to be lower than for a bare substrate with $\kappa=\kappa_{sub}$. This is verified by numerical integration.

From these results, we note that the use of 2-layer model is especially relevant only for layers much thinner than w ($\ll 450$ nm in the experiments presented in this work) and when the thermal conductivity of the top layer is much smaller than that of the substrate, which is also the case for alloy epilayers.

4. TE parameters modelling

The electron conductivity σ, Seebeck coefficient S, and electron thermal conductivity κ_e were calculated using the conventional expressions, e.g. see Ref.[3]. The density of states and electron velocity, required in these expressions, are calculated from the band structure, and in this work we have used 8-band k.p model for the conduction band dispersion around Γ point, while the effective mass description was used for L valley. The material parameters for GeSn alloys were taken according to the quadratic expressions from [4], more accurate than the simple weighted-average. The carrier scattering was calculated with acoustic phonon, deformation potential, intervalley, alloy disorder, ionized impurity, and point defects scattering included. The relaxation times were calculated from the conventional expressions,[5,6] using the parameters for Ge[7] for phonon-related processes, which is a reasonable approximation for Ge-rich alloys. The ionized impurity scattering was calculated according to Brooks-Herring model (Eq.(9)-(11) from[5]). The alloy disorder

scattering was calculated using Eq.(8) from[5], and the scattering potential U was taken as the difference of band edges in bulk Ge and Sn for the particular type of electrons (Γ or L), i.e. it is taken as $U=0.69eV+E_{g,Sn}-E_{g,Ge}$, where $E_{g,Sn}$ and $E_{g,Ge}$ are the corresponding band gaps. This is just a rough approximation, but still reasonable for estimation purposes, because we do not know of any more detailed investigation of alloy scattering potential in GeSn alloys. The scattering on neutral point defects was calculated with the binding energy $E_T=0.5$ meV, as given in Ref.[8] for Ge.

References

(1) Cahill, D. G. Analysis of Heat Flow in Layered Structures for Time-Domain Thermoreflectance. *Review of Scientific Instruments* **2004**, *75* (12), 5119–5122. https://doi.org/10.1063/1.1819431.

(2) Stoib, B.; Filser, S.; Stötzel, J.; Greppmair, A.; Petermann, N.; Wiggers, H.; Schierning, G.; Stutzmann, M.; Brandt, M. S. Spatially Resolved Determination of Thermal Conductivity by Raman Spectroscopy. *Semicond. Sci. Technol.* **2014**, *29* (12), 124005. https://doi.org/10.1088/0268-1242/29/12/124005.

(3) Sztein, A.; Haberstroh, J.; Bowers, J. E.; DenBaars, S. P.; Nakamura, S. Calculated Thermoelectric Properties of InxGa1−xN, InxAl1−xN, and AlxGa1−xN. *Journal of Applied Physics* **2013**, *113* (18), 183707. https://doi.org/10.1063/1.4804174.

(4) Liu, S.-Q.; Yen, S.-T. Extraction of Eight-Band k · p Parameters from Empirical Pseudopotentials for GeSn. *Journal of Applied Physics* **2019**, *125* (24), 245701. https://doi.org/10.1063/1.5099073.

(5) Fu, Y.; Joelsson, K. B.; Grahn, K. J.; Ni, W.-X.; Hansson, G. V.; Willander, M. Hall Factor in Strained P-Type Doped $Si_{1-x}Ge_x$ Alloy. *Phys. Rev. B* **1996**, *54* (16), 11317–11321. https://doi.org/10.1103/PhysRevB.54.11317.

(6) Jacoboni, C.; Reggiani, L. The Monte Carlo Method for the Solution of Charge Transport in Semiconductors with Applications to Covalent Materials. *Rev. Mod. Phys.* **1983**, *55* (3), 645–705. https://doi.org/10.1103/RevModPhys.55.645.

(7) Murphy-Armando, F.; Fahy, S. Giant Enhancement of N-Type Carrier Mobility in Highly Strained Germanium Nanostructures. *Journal of Applied Physics* **2011**, *109* (11), 113703. https://doi.org/10.1063/1.3590334.

(8) Ridley, B. K. *Quantum Processes in Semiconductors*; Clarendon Press: Oxford, 1999.